Understanding and predicting profile structure and parametric scaling of intrinsic rotation

W. X. Wang, , B. A. Grierson, , S. Ethier, , J. Chen, , E. Startsev, and , and P. H. Diamond

Citation: Physics of Plasmas **24**, 092501 (2017); doi: 10.1063/1.4997789

PHYSICS OF PLASMAS **24**, 092501 (2017)

Understanding and predicting profile structure and parametric scaling of intrinsic rotation

W. X. Wang,[1,a),b)] B. A. Grierson,[1] S. Ethier,[1] J. Chen,[1] E. Startsev,[1] and P. H. Diamond[2]
[1]*Plasma Physics Laboratory, Princeton University, P.O. Box 451, Princeton, New Jersey 08543, USA*
[2]*University of California, San Diego, La Jolla, California 92093, USA*

(Received 26 April 2017; accepted 23 July 2017; published online 10 August 2017)

This paper reports on a recent advance in developing physical understanding and a first-principles-based model for predicting intrinsic rotation profiles in magnetic fusion experiments. It is shown for the first time that turbulent fluctuation-driven residual stress (a non-diffusive component of momentum flux) along with diffusive momentum flux can account for both the shape and magnitude of the observed intrinsic toroidal rotation profile. Both the turbulence intensity gradient and zonal flow $\mathbf{E} \times \mathbf{B}$ shear are identified as major contributors to the generation of the $k_{\|}$-asymmetry needed for the residual stress generation. The model predictions of core rotation based on global gyrokinetic simulations agree well with the experimental measurements of main ion toroidal rotation for a set of DIII-D ECH discharges. The validated model is further used to investigate the characteristic dependence of residual stress and intrinsic rotation profile structure on the multi-dimensional parametric space covering the turbulence type, q-profile structure, and up-down asymmetry in magnetic geometry with the goal of developing the physics understanding needed for rotation profile control and optimization. It is shown that in the flat-q profile regime, intrinsic rotations driven by ITG and TEM turbulence are in the opposite direction (i.e., intrinsic rotation reverses). The predictive model also produces reversed intrinsic rotation for plasmas with weak and normal shear q-profiles. *Published by AIP Publishing*. [http://dx.doi.org/10.1063/1.4997789]

I. INTRODUCTION

Plasma flows, toroidal rotation in particular, can play an important role in controlling plasma macro-stability and improving confinement performance. Toroidal rotation is often driven externally through neutral beam injection (NBI) in current fusion experiments. However, in future large size devices, the beam torque relative to the moment of inertia of the plasma will be much smaller than the present experiments. Therefore, ITER, for example, may have to rely on plasma self-generated intrinsic rotation for controlling plasma stability and microturbulence.

It is generally believed that there are two key elements for the generation of intrinsic rotation. The first one is edge momentum sources and sinks, which can be caused by various processes and mechanisms near the plasma boundary, such as direct particle losses through the last closed magnetic surface to the scrape-off layer (SOL),[1] transport imbalance between trapped and passing particles coupling with edge geometry effects,[2] boundary stresses,[3] and SOL flows.[4] The second key element is momentum transport, which can bring the edge momentum, either positive or negative, into the core region, redistribute it, and form a global rotation profile. In particular, a non-diffusive momentum flux which connects edge momentum sources/sinks and core plasma flow is critical. Plasma turbulence provides a key mechanism for driving toroidal momentum transport. The radial flux of toroidal angular momentum due to turbulence consists, in general, of three components as expressed below

$$\Gamma_{r,\phi} \propto -c_1\chi_\phi \frac{\partial V_\phi}{\partial \rho} + c_2 V_p V_\phi + \Pi^{rs}_{r,\phi},$$

e.g., the usual momentum diffusion (first term) and two non-diffusive momentum fluxes which are momentum pinch (second term) and residual toroidal Reynolds stress (third term). Here, χ_ϕ and V_p denote the momentum diffusivity and pinch velocity, respectively; ρ denotes radial coordinates (a label of the flux surface); and V_ϕ is the toroidal rotation velocity. The three components in the turbulence-driven momentum flux have different physics origins and have distinct effects on global profile formation. The diffusive transport is well known in the direction opposite to the rotation gradient, leading to the relaxation of the rotation profile. The momentum pinch term is a convective flux, which can transport momentum in either direction, up-gradient or down-gradient. The residual stress is defined as a specific part of the Reynolds stress, which does not directly depend on the rotation velocity and its gradient. A spatially non-uniform residual stress provides a source for intrinsic torque and intrinsic rotation in the sense that it allows plasma to spin up from rest.

After more than a decade of intensive experimental, theoretical, and computational studies leading to significant progress in understanding the intrinsic rotation phenomenon, one central question raised by the fusion community [e.g., from recent Transport & Confinement Topical Group meetings of International Tokamak Physics Activity (ITPA)] is if we have enough knowledge and valid modeling capability for intrinsic rotation prediction.[5] This paper presents an effort to address this issue. Progress in this direction significantly lags behind the progress in predicting other plasma profiles such

---

Note: Paper PI3 6, Bull. Am. Phys. Soc. **61**, 281 (2016).
[a)] Invited speaker.
[b)] wwang@pppl.gov

as temperature and density. As a distinct feature, momentum transport is highly non-diffusive, which plays a critical role in the formation of the rotation profile. With regard to intrinsic rotation prediction, both its achievable amplitude and profile structure are important since each one may result in different effects on macro- and micro-instabilities. The highly non-diffusive nature in toroidal momentum transport gives rise to more complex profile structures of toroidal rotation relative to the temperature profile. Phenomenologically, intrinsic toroidal rotation exhibits more often non-monotonic profiles, profile reversals, etc. A related interesting question is whether a transport barrier exists for toroidal rotation (if yes, the underlying dynamics appears more complicated than that for the barriers of temperature, for which the profile is mostly determined by the diffusive transport process).

The rest of this paper is organized as follows: In Sec. II, a brief description of DIII-D rotation experiments and gyrokinetic simulations used for this study is given, and general features of turbulence-driven momentum transport in these DIII-D plasmas obtained from gyrokinetic simulations are presented. In Sec. III, a first-principles-based predictive model is discussed, and the results of predictions of intrinsic rotation for DIII-D ECH discharges are presented. In Sec. IV, the predictive model is further used to investigate the characteristic dependence of the residual stress and intrinsic rotation profile structure on the multi-dimensional parametric space with the goal of developing the physics understanding needed for rotation profile control and optimization. A summary is given in Sec. V.

II. CHARACTERISTICS OF TURBULENCE-DRIVEN MOMENTUM TRANSPORT IN ECH PLASMAS

Understanding and predicting the intrinsic rotation profile structure present a great challenge and opportunity to test the physics of turbulence-driven intrinsic rotation and validate the first-principles-based models. In this paper, we focus on electron-heated plasmas without momentum torque injection for our study. A set of DIII-D deuterium discharges heated by electron cyclotron waves (ECH) with different ECH input powers are simulated using global nonlinear gyrokinetic simulations. Figure 1 shows how plasma profiles of density, electron temperature, ion temperature, and toroidal rotation change as the ECH power increases. More detailed descriptions of these experiments and measurements are given in Ref. 6. The toroidal rotations observed in those discharges are essentially the plasma self-generated intrinsic rotation since the momentum torque associated with ECH injection is negligible. We use those ECH discharges for this study for several reasons. First, ECH discharges are quite relevant to ITER since ECH power directly goes to electrons and ITER plasmas are expected to be dominated by electron heating. Second, intrinsic rotations observed in those ECH plasmas show very interesting features in global profile structures. Specifically, they are non-monotonic with an off-axis peak in the core region. A core-hollowing rotation profile was also observed in off-axis ECH-heated helium discharges on DIII-D.[7,8] Such off-axis peaked, non-monotonic profiles cannot be generated through a pure momentum diffusion process, and it is a clear indication of the importance of non-diffusive momentum transport. One unique feature of those DIII-D experiments is that the measurements of toroidal rotation are directly obtained from bulk ions of helium[8] and deuterium[9,10] rather than merely from impurities as in most previous experiments. Finally, these well-diagnosed DIII-D discharges provide high fidelity experimental plasma profiles, which is critical for the purpose of validation.

In this work, our global turbulence simulation studies are carried out using the Gyrokinetic Tokamak Simulation (GTS) code.[11,12] The GTS code performs gradient-driven turbulence simulation based on a generalized gyrokinetic simulation model using a δf particle-in-cell approach. GTS simulations of DIII-D discharges for this study take into account the comprehensive influence of many physics effects, including fully kinetic electrons, realistic geometry constructed using experimental data, real electron and ion collisions, toroidal flow, and equilibrium electric field. All the plasma profiles and the equilibrium radial electric field are directly read from experimental database. Global simulations cover a wide region of

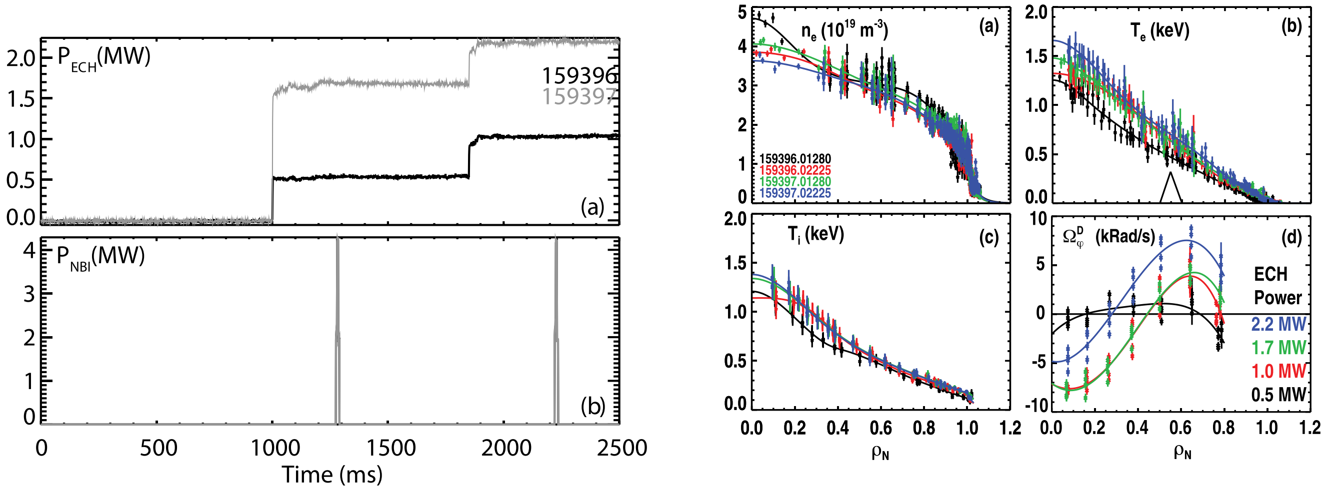

FIG. 1. Time history of ECH power and short neutral beam pulses (for the main ion rotation measurement) (left) and radial profiles of n_e, T_e, T_i, and ion toroidal rotation (right) from the DIII-D ECH power scan experiments.

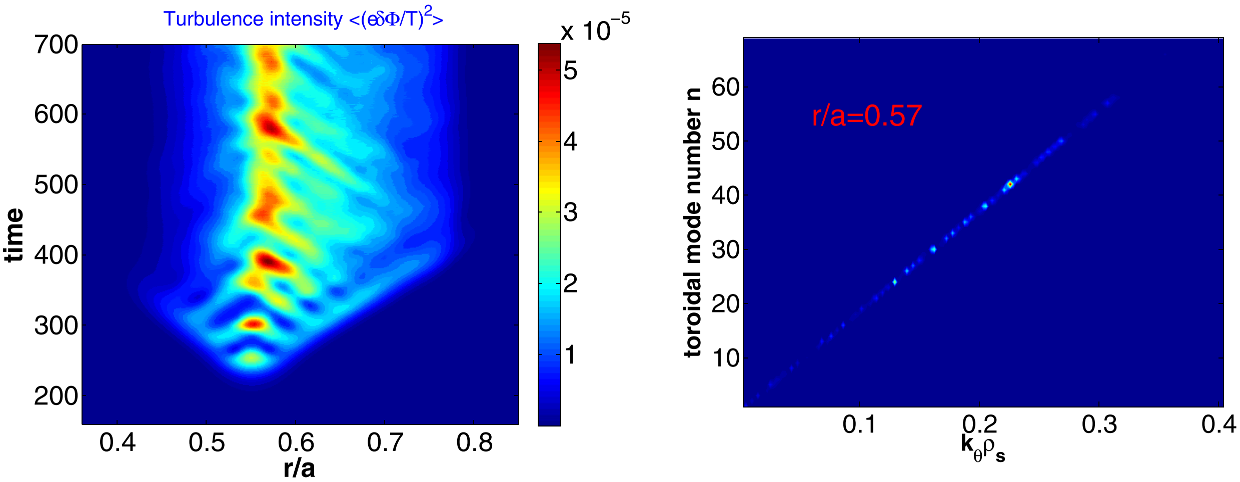

FIG. 2. Spatiotemporal evolution of the turbulence intensity (left) and potential fluctuation spectrum at a minor radius $r/a = 0.57$ (right). The time on the left plot is normalized by $L_{T_i}/v_{th,i}$, the ratio of the ion temperature gradient scale length, and ion thermal velocity.

minor radii, from $r/a = 0.05$ to 0.9. A large number of simulation particles (60–100 particles per cell per species) are used in order to achieve good statistics. The spatial grid size in the perpendicular direction is approximately equal to or less than the local ion gyroradius ρ_i. The wavenumber range that is simulated is $k_\perp\rho_i \lesssim 2$, which covers the typical low-k turbulence due to ion temperature gradient (ITG) mode and trapped electron mode (TEM).

In order to separate the three components of the toroidal momentum flux, three independent, nonlinear simulations are performed for each experimental discharge, using zero toroidal rotation, a rigid toroidal rotation, and the realistic toroidal rotation profile, respectively. Correspondingly, the simulated toroidal momentum fluxes in the three simulations are, by definition, purely residual Reynolds stress, both residual stress and momentum pinch, and all three components. It is important that the three simulations use the same equilibrium radial electric field which comes from experimental data. This assures that underlying turbulence and fluctuations for driving residual stress, momentum pinch, and diffusion are roughly identical when calculating each component of the momentum flux and that the underlying turbulence and fluctuations correspond to that of the specific experimental case being considered. On the other hand, for a typical intrinsic rotation, the rotation profile is well below the threshold for exciting Kelvin-Helmholtz instability.[13] Therefore, the use of three different toroidal rotations produces negligible influence on the simulated turbulence but allows us to calculate residual stress, pinch, and diffusion separately in the same turbulence state corresponding to the experimental discharge being considered.

Because of the relatively low temperature and sufficiently high density of those ECH discharges, there is strong collisional coupling between electron and ion species, such that electron cyclotron resonance heating raises both electron and ion temperatures through collisional energy exchange. Therefore, direct electron heating in these plasmas increases both electron and ion pressure gradients that can drive instabilities. The simulation results show that significant turbulent fluctuations, which are mainly driven by ion temperature gradient (ITG) instabilities, are present in the core region of those DIII-D ECH discharges from 0.4 to 0.8 in the minor radius. The spatiotemporal evolution of turbulence intensity, defined as $\langle (e\delta\Phi/T_i)^2\rangle$ with $\delta\Phi$ and T_i being the potential fluctuation and ion temperature, respectively, is displayed in the left panel of Fig. 2, which shows that fully developed turbulent fluctuations peak at around $r/a = 0.55-0.6$, close to the location of the rotation profile peak. The simulated turbulence is dominated by low-k fluctuations with normalized poloidal wavenumber $k_\theta\rho_s \sim 0.1-0.3$, and correspondingly, dominated by toroidal mode numbers from 20 to 60 (the right panel of Fig. 2). It is not surprising that the modes of saturated fluctuations are observed to cluster along the line of a resonant surface in the wavenumber (m, n)-space, which is specified by $m/n = q(r)$. Here, (m, n) are the poloidal and toroidal mode numbers, respectively, and $q(r)$ is the safety factor.

Before further discussion of the physics results, it is interesting to examine the property of toroidal momentum conservation in our gyrokinetic simulations. Figure 3 plots

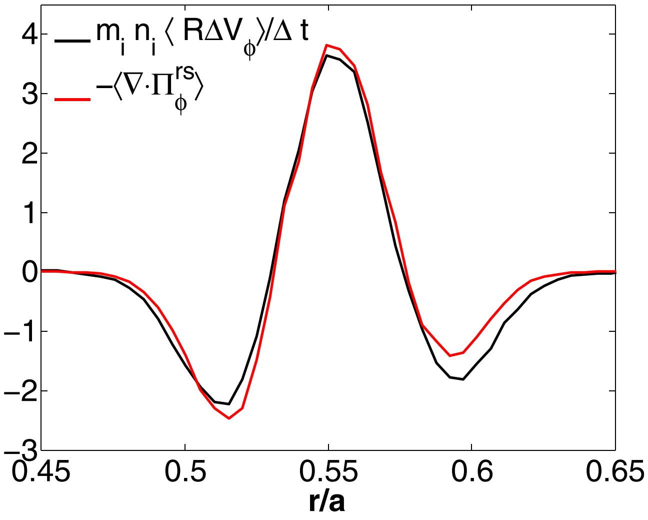

FIG. 3. Radial profile of the toroidal momentum change rate $\sim\Delta V_\phi/\Delta t$ and intrinsic torque density $\sim -\langle\nabla\cdot\mathbf{\Pi}_\phi^{rs}\rangle$ due to residual stress from the same simulation of Fig. 2 using no toroidal rotation.

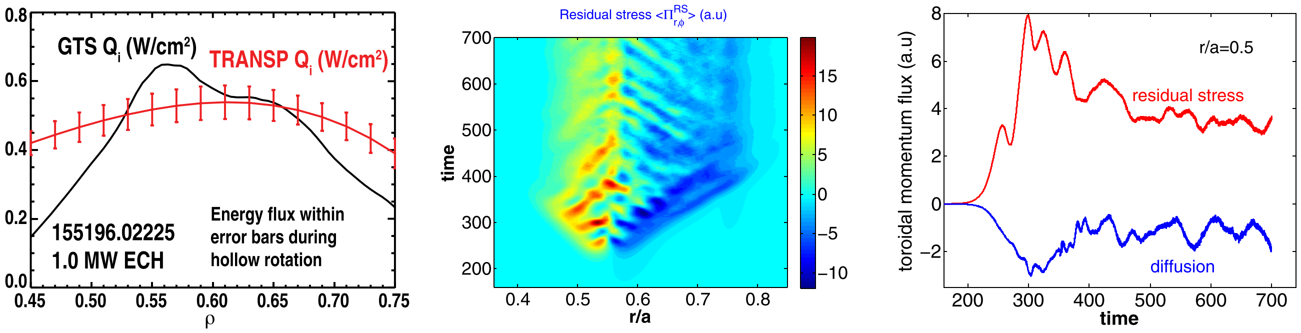

FIG. 4. Radial profile of simulated turbulence-driven ion energy flux compared with experimental values from TRANSP analysis (left); spatiotemporal evolution of simulated residual stress (middle); and time history of residual stress and diffusive momentum flux at $r/a = 0.5$ (left) for a DIII-D ECH discharge. The time on the middle and right plots is normalized by $L_{T_i}/v_{th,i}$.

the rate of toroidal momentum change and the divergence of residual stress (namely, fluctuation-driven intrinsic torque) during a phase of turbulence development from the simulation using no toroidal rotation. These correspond to the two terms in the following local momentum conservation equation (with no diffusion and pinch in the momentum flux, respectively),

$$\frac{\partial}{\partial t}\left(m_i n_i \langle R V_\phi \rangle\right) + \langle \nabla \cdot \mathbf{\Pi}^{\mathrm{rs}}_\phi \rangle = 0. \tag{1}$$

Here, R, m_i, and n_i are the major radius, ion mass, and density, respectively. The two curves are on the top of each other, indicating that the local momentum conservation is well satisfied.

The ITG turbulence in these ECH plasmas is found to drive a significant anomalous thermal transport of the experimental level as shown in the left of Fig. 4 which compares the ion energy flux between simulation and experiments in the core region. In addition, the turbulence is also found to drive a substantial, quasi-stationary toroidal momentum flux in the core region in the situation of zero toroidal rotation, as shown in the middle and right of Fig. 4. The radial flux of ion toroidal momentum is calculated in the simulations according to $\langle \mathbf{\Gamma}_\phi \cdot \nabla\rho \rangle \equiv \langle \int d^3 v m_i R v_\phi (\mathbf{v}_E \cdot \nabla\rho)\delta f_i \rangle$, where v_ϕ and $\mathbf{v}_E$ are the toroidal velocity and turbulence-perturbed $\mathbf{E} \times \mathbf{B}$ velocity, respectively; δf_i is the turbulence perturbation of the ion distribution function; and $\langle\ \rangle$ denotes the flux surface average. In the situation of no toroidal rotation, the simulated momentum flux is merely the residual stress $\langle \mathbf{\Pi}^{\mathrm{rs}}_\phi \cdot \nabla\rho \rangle$ by definition (because V_ϕ and its gradient are zero). The amplitude of the residual stress is seen to be comparable to that of momentum diffusion in Fig. 4.

One outstanding feature of turbulence-driven residual stress found here shows an anti-gradient, dipole structure, as illustrated in Fig. 5, which plots the steady-state radial profile of residual stress, diffusive momentum flux, and the sum of residual stress and momentum pinch calculated using the three simulations described previously. As is generally done for calculating transport fluxes in this type of turbulence simulation studies where simulations are run well beyond the linear growth phase of the instability to reach a well-saturated, stationary turbulence state, the momentum flux profiles plotted in Fig. 5 are obtained by time average in the saturated turbulence state over a long period. Generally, the interval of time averaging should be some time scale between the correlation time and the profile evolution time. More specifically, an averaged transport flux is calculated over a period of many turbulence growth times.

As shown in the figure, the simulated residual stress (red curve in Fig. 5) is found to switch sign at $r/a \sim 0.6$. On the other hand, the simulated turbulence-driven momentum diffusion (blue curve in Fig. 5) is shown to follow the gradient, as it should be. The black curve represents the sum of residual stress and momentum pinch, which is obtained from the simulation using a finite, uniform rotation frequency. The result that the black curve is almost on the top of the residual stress profile indicates that the momentum pinch due to turbulence is negligibly small. The anti-gradient, dipole structure in the residual stress is found to be critical for the formation of the off-axis-peaked core rotation profile observed in ECH experiments. As shown in Fig. 5, the momentum flux associated with the residual stress is outward in the inner core region and inward in the outer core region, which provides a counter-balance against the momentum diffusion. This is exactly what is needed in order to hold a steady state off-axis-peaked core rotation profile.

We now discuss the physics mechanisms driving the residual stress. A major contribution to the residual stress is parallel Reynolds stress $\langle \tilde{v}_r \tilde{v}_\parallel \rangle$, which needs a finite parallel

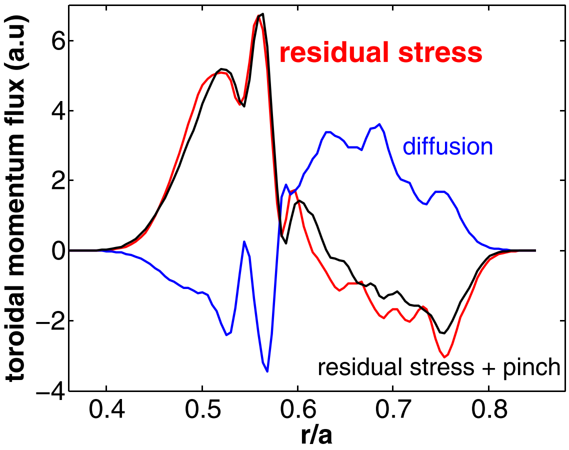

FIG. 5. Radial profile of simulated residual stress, momentum diffusion, and the sum of residual stress and momentum pinch at the steady state.

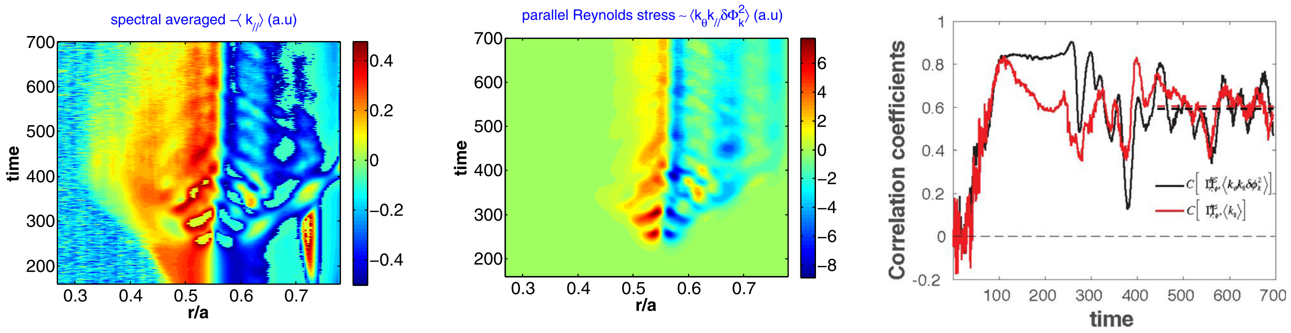

FIG. 6. Spatiotemporal evolution of spectral averaged $\langle k_\parallel \rangle$ (left), parallel Reynolds stress based on the quasi-linear estimate (middle), and correlation coefficients of simulated toroidal residual stress with $\langle k_\parallel \rangle$ and the parallel Reynolds stress (right).

wave number $k_\parallel$ (on average) to be nonvanishing.[14] Indeed, our simulation results confirm that the toroidal residual stress is generally dominated by the parallel Reynolds stress. For most drift-wave instabilities, the modes with positive and negative $k_\parallel$ are equally excited in ideal situations. Namely, there is a perfect reflection symmetry in the $k_\parallel$ spectrum and a zero average $k_\parallel$. Therefore, a critical factor for turbulence to drive residual stress is the presence of physics effects which can break $k_\parallel$-symmetry. Several physics mechanisms that may cause such symmetry breaking and thus the generation of residual Reynolds stress have been studied. These include finite shear in the $\mathbf{E} \times \mathbf{B}$ velocity,[15,16] turbulence self-generated low frequency zonal flow shear,[17] up-down asymmetry in equilibrium geometry,[18] radial gradient in the turbulence intensity,[19] poloidal tilt of the global mode structure,[20] and diamagnetic level velocity shear[21] arising from the profile shearing and magnetic shear effects on the turbulence spectrum.[22] Most of these mechanisms are enabled in the presence of global turbulence effects. Higher order terms in the gyrokinetic equation are also being investigated as possible drivers, which are needed to break the structural symmetry of gyrokinetics in the local flux-tube limit[23] and then produce residual stress (which otherwise vanishes because of the structural symmetry in the local limit).

The GTS simulations used for this study take into account the global turbulence effects and the effect of up-down geometric asymmetry needed for symmetry breaking and turbulence-driven toroidal momentum flux. Such global effects have proven to be significant for turbulence to drive residual stress in many previous gyrokinetic studies. The left panel of Fig. 6 displays the spatiotemporal evolution of spectrum-averaged $k_\parallel$ defined as[17]

$$\langle k_\parallel \rangle (r) \equiv \frac{1}{qR_0} \frac{\sum (nq - m)\delta\Phi_{mn}^2}{\sum \delta\Phi_{mn}^2},$$

where Φ_{mn} is the mode amplitude of the Fourier component of the mode number (m, n), and R_0 is the major radius. It clearly shows the generation of significant finite $k_\parallel$ due to symmetry breaking in saturated turbulence. The radial profile of the averaged $k_\parallel$ shows a dipole structure which is consistent with the dipole structure observed in the directly calculated residual toroidal Reynolds stress (see Fig. 4). In the middle panel of Fig. 6, a parallel Reynolds stress estimated via $\langle \tilde{v}_r \tilde{v}_\parallel \rangle \sim \langle k_\theta k_\parallel \delta\phi_k^2 \rangle$ in terms of the quasi-linear theory shows a similar spatiotemporal structure as the directly simulated residual stress (see the middle of Fig. 4). Further quantitative analysis indeed shows strong correlations of the toroidal residual stress with the spectrum-average $k_\parallel$ and the parallel Reynolds stress in the steady state turbulence phase (the right panel of Fig. 6).

Further investigation is carried out to identify the cause of $k_\parallel$-symmetry breaking needed for generating residual stress among various mechanisms previously mentioned. First, it is quite suggestive that the spatiotemporal structure of the turbulence self-generated zonal flow shearing rate $\gamma_{\mathrm{E\times B}}^{\mathrm{ZF}}$ and fluctuation intensity gradient $d\langle \delta\Phi^2 \rangle / d\rho$ (the left and middle of Fig. 7) looks similar to that of the spectral averaged $k_\parallel$. The zonal flow shearing rate is calculated

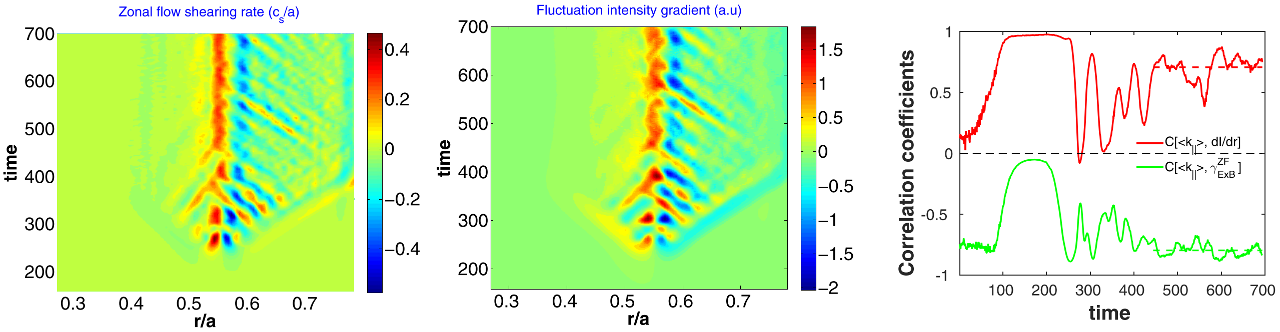

FIG. 7. Spatiotemporal evolution of the zonal flow shearing rate (left) and turbulence intensity gradient (middle) and the time history of correlation coefficients of spectral averaged $\langle k_\parallel \rangle (r)$ with the turbulence intensity gradient and zonal flow shearing rate (right). Note that the absolute value of the correlation coefficient measures the correlation strength.

according to $\gamma^{\rm ZF}_{\rm E\times B} = \frac{R^2B_p^2}{B}\frac{\partial}{\partial\Psi_p}\left(\frac{E^{\rm ZF}}{RB_p}\right)$,[24] where B and B_p are the total and poloidal magnetic field strengths, and Ψ_p is the poloidal magnetic flux. Indeed, the strongest correlations are found for $\langle k_\parallel\rangle$ with both of them as shown in the right panel of Fig. 7, which displays the correlations of three radial profiles: $\langle k_\parallel\rangle$ vs. $d\langle\delta\Phi^2\rangle/d\rho$ and $\langle k_\parallel\rangle$ vs. $\gamma^{\rm ZF}_{\rm E\times B}$ as a function of time. This result suggests that both the turbulence intensity gradient and zonal flow $\mathbf{E}\times\mathbf{B}$ shear are major contributors to the $k_\parallel$-symmetry breaking needed for residual stress generation. On the other hand, the effect of equilibrium $\mathbf{E}\times\mathbf{B}$ shear is shown to be less significant compared to that of zonal flow. Here, the simulation is performed using the up-down symmetry equilibrium, and thus, there is no contribution to $k_\parallel$-symmetry breaking due to up-down asymmetry effects. The simulation using the up-down asymmetric equilibrium is also performed which, however, results in minor differences in the calculated residual stress and the prediction of the intrinsic rotation profile, indicating that the effect of up-down asymmetry equilibrium on $k_\parallel$-symmetry breaking is not important in those plasmas. This result is presented in more detail in Sec. III. The up-down asymmetry in the biased poloidal tilt of the global mode structure due to equilibrium profile shearing may lead to $k_\parallel$-symmetry breaking. However, this eigenmode feature appears mostly in the linear phase and the poloidal tilt is largely diminished by nonlinear physics, such as the zonal flow shearing effect. Therefore, its effect on $k_\parallel$-symmetry breaking is weakened in the fully developed turbulence state. Finally, the magnetic shear effect on the turbulence spectrum also provides a mechanism for $k_\parallel$-symmetry breaking by causing a radial shift of poloidal harmonics. However, this effect is significant in the low magnetic shear regime and appears weak in those ECH plasmas which have normal magnetic shear in the core region.

As one prominent feature, the simulated turbulence and transport of these DIII-D ECH plasmas are characterized by burstings, which emerge regularly in time and ballistically propagate in the radial direction, as shown by the strip structures in the spatiotemporal evolution of various observables including turbulence intensity, transport fluxes (e.g., residual stress), zonal flows, etc. Such avalanche-like events are widely observed in various type of gyrokinetic turbulence simulations.[12,25–28] These include flux- and gradient-driven turbulence simulations and global and local simulations. The quasi-periodic excitation of burstings and avalanches appear due to the dynamical interplay between turbulence-driven transport fluxes and local plasma profile modulations. For the DIII-D ECH case simulated here, the avalanches are initialized in both the left and right sides (near $r/a = 0.4$ and 0.8) of the turbulence region, where the local ion temperature gradient is dynamically enhanced due to turbulence-induced thermal transport. In contrast, the local ion temperature gradient is mostly weakened in the central area of the turbulence region. The avalanches propagate radially toward the center of the region near the deposition peak of ECH (see, for example, the middle of Fig. 4). Radially inward propagating avalanches in the outer side of the turbulence region appear stronger (with a larger size and amplitude). As suggested by the previous studies, the characteristics of avalanches appear to closely depend on the underlying zonal flow dynamics. Figure 8 shows the radial profile of the total $\mathbf{E}\times\mathbf{B}$ shearing rate including contributions from both the turbulence self-generated zonal E_r and the equilibrium E_r. The zonal flow $\mathbf{E}\times\mathbf{B}$ shearing rate is obtained by time-averaging the left plot of Fig. 7 in the stationary turbulence phase from $t = 400$ to 700. The zonal flow shear is shown to be dominant in this case. The sign of the total $\mathbf{E}\times\mathbf{B}$ shear switches at a radial location near the deposition peak of ECH. The propagation direction of avalanches shows a close dependence on the sign of the $\mathbf{E}\times\mathbf{B}$ shear. This is consistent with the observations of the previous simulations. This dependence is established through (i) the radial propagation mechanism of tilted turbulence due to $\mathbf{E}\times\mathbf{B}$ shear[27] and (ii) the $\mathbf{E}\times\mathbf{B}$-shear-mediated directional mode coupling.[28] Furthermore, the radial extent of avalanches is bounded by the radial scale of $\mathbf{E}\times\mathbf{B}$ shear with the same sign. More specifically, the radial extend of the avalanches in the outer region ($r/a > 0.55$) is about $60\rho_i$. The avalanche propagation velocity is estimated to be $(2-3)\rho_i v_{th,i}/R$, and the estimated avalanche frequency is $\sim 0.9 v_{th,i}/R$ which is lower than the GAM frequency. All these are consistent with the results of previous simulations.[12,27,28]

Avalanche-like radial-temporal structures are widely observed in turbulence simulations. It would be interesting to identify such structures in fusion experiments in order to validate the associated physics and simulation results and further to study the effect of the avalanche-type non-diffusive transport process on plasma confinement. Turbulence-driven particle flux may be directly measured with a heavy ion beam probe. The data of particle flux measured at two or more radial locations may allow to search for the long range radial correlation (much longer than the turbulence correlation length) that characterizes the avalanche-like transport. However, it is generally more difficult to detect such structures in transport fluxes than in potential, density, and temperature fluctuations. The electron cyclotron emission (ECE) and reflectometer diagnostic for fluctuation measurements may have relevant temporal and spatial resolution for this purpose. Beam emission spectroscopy (BES) should be another diagnostic that may be able to measure the large

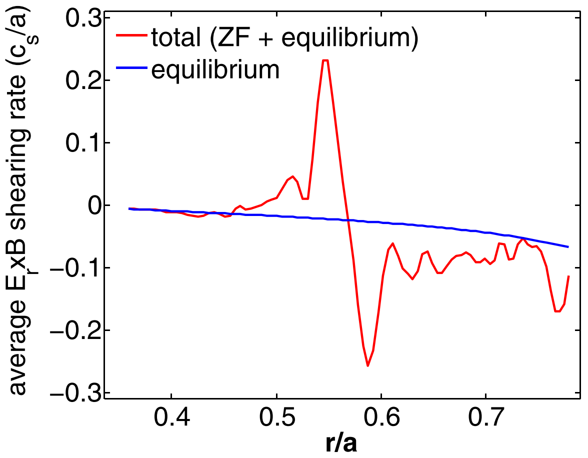

FIG. 8. Radial profile of the time-averaged total $\mathbf{E}\times\mathbf{B}$ shearing rate. Also plotted is the equilibrium $\mathbf{E}\times\mathbf{B}$ shearing rate (blue curve).

density fluctuation structure with good temporal resolution. Actually, avalanche-like phenomena are detected in experiments in both the edge and the SOL region using Langmuir probes[29] and a wide cross section of the plasma using the ECE measurement.[30] The power spectra of electrostatic potential, density, and electron temperature fluctuations are found to exhibit f^{-1}-scaling, which is a fingerprint of avalanche-like phenomena associated with self-organized criticality (SOC).[31] The radial propagation of avalanches is also observed. In particular, the effective radial propagation velocity is estimated from the ECE data of T_e fluctuations to be 2 orders of magnitude below the sound speed in the DIII-D core plasmas.[30] This is within the same range of our simulated avalanche propagation velocity for the DIII-D ECH discharges [$\sim(2-3)\rho_i v_{th,i}/R \sim \rho^* c_s$]. However, for the DIII-D ECH experiments of intrinsic rotation studied here, BES measurements were not available as the BES beams can strongly disturb intrinsic rotation, and we do not have sufficient fluctuation data needed for the search of evidence of avalanche-like structures as suggested by our simulations. Nevertheless, this will be a highly interesting issue for future studies.

III. FIRST-PRINCIPLES-BASED MODEL AND INTRINSIC ROTATION PREDICTION

We have shown that a significant residual stress is generated by ITG turbulence in these ECH plasmas. However, how does residual stress affect the formation of the global rotation profile? We now discuss a first-principles-based model for intrinsic rotation prediction, which will also help clarify this question. We start from the ion toroidal angular momentum transport equation in the absence of external torque and neglect the torque from neoclassical toroidal viscosity in the presence of broken toroidal symmetry in magnetic geometry

$$\frac{\partial}{\partial t}\left(m_i n_i \langle R V_\phi \rangle\right) + \langle \nabla \cdot \mathbf{\Gamma}_\phi \rangle = 0, \tag{2}$$

where $\mathbf{\Gamma}_\phi \equiv \int d^3 v m_i R v_\phi \mathbf{v}_E \delta f_i$ is the total toroidal angular momentum flux. The steady state condition (also taking into account boundary conditions) requires

$$\langle \mathbf{\Gamma}_\phi \cdot \nabla \rho \rangle \propto -c_1 \chi_\phi \frac{\partial V_\phi}{\partial \rho} + c_2 V_p V_\phi + \Pi^{\mathrm{rs}}_{r,\phi} = 0.$$

This equation states that at the steady state, the plasma will self-organize to form a global intrinsic rotation profile so as to make the total momentum flux vanish everywhere radially. We have shown that the turbulence-produced momentum pinch is small (negligible). Thus, the steady state equation reduces to the balance between momentum diffusion and residual stress:

$$m_i n_i \chi_\phi(\rho) \langle R^2 |\nabla \rho|^2 \rangle \frac{d\omega_\phi}{d\rho} = \Pi^{\mathrm{rs}}_{r,\phi} \left(\equiv \langle \mathbf{\Pi}^{\mathrm{rs}}_\phi \cdot \nabla \rho \rangle\right). \tag{3}$$

Here, ω_ϕ is the toroidal rotation frequency. This is a one-dimensional ordinary differential equation for determining the intrinsic rotation profile when the residual stress $\Pi^{\mathrm{rs}}_{r,\phi}$, momentum diffusivity χ_ϕ, and a boundary condition are given. The first-principles-based global gyrokinetic simulation provides the residual stress on the right hand side. The momentum diffusivity χ_ϕ, in principle, is unknown since in order to calculate χ_ϕ using gyrokinetic simulations, we need to know the toroidal rotation which, however, is what we want to predict. Moreover, in the presence of a region of flat toroidal rotation, χ_ϕ cannot be determined. Instead, we use the well-known relation, $\chi_\phi(\rho) = P_r \chi_i(\rho)$, to relate χ_ϕ with the thermal diffusivity χ_i, which can be obtained by our gyrokinetic simulations without using the toroidal rotation as an input (but keeping the same equilibrium electric field from TRANSP analysis). Here, P_r is the intrinsic Prandtl number, which is well established both theoretically and experimentally, with a value close to or less than unity.[32,33] With regard to the boundary condition needed for solving the equation, we directly use the experimentally measured toroidal rotation frequency ω_ϕ in the edge region, which is determined by edge physics near open field lines and outside the scope of this study.

The range of the Prandtl number associated with turbulence has been extensively studied both theoretically and experimentally. We should stress that the choice of the Prandtl number in our predictive model is not arbitrary but based on our simulation results for justification. Figure 9 shows the simulated χ_i and χ_ϕ for the DIII-D ECH discharge. We can see that χ_ϕ is slightly smaller than χ_i in regions of the finite rotation gradient, where χ_ϕ is well defined. On average, the Prandtl number, χ_ϕ/χ_i, is about $P_r = 0.7$, which is also consistent with the results of previous studies.[33,34] A typical Prandtl value $\mathrm{Pr} = 0.7$ is widely used in such studies of intrinsic rotation (see, for instance, Ref. 35). We should clarify that, in Fig. 9, the simulation uses experimental toroidal rotation as input for calculating momentum diffusivity, the purpose of which is to validate that the Prandtl number in those DIII-D ECH plasma conditions indeed falls into the range of the Prandtl number, which has been established theoretically. This average Prandtl number as expected is then used in the predictive model to calculate the toroidal rotation.

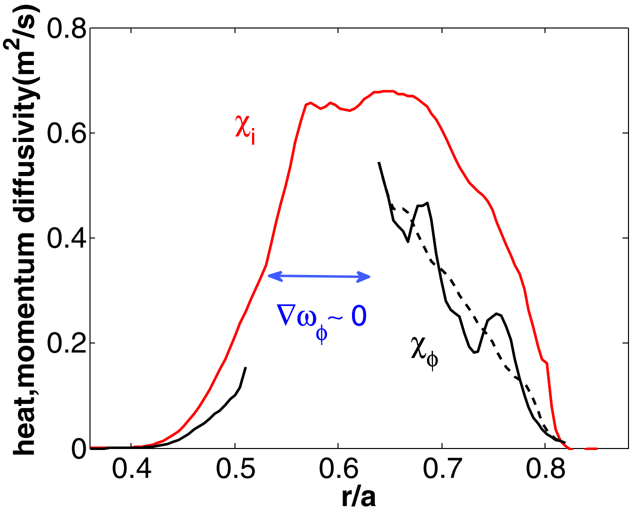

FIG. 9. Radial profiles of simulated ion heat and momentum diffusivity for the DIII-D ECH plasma, indicating a Prandtl number $P_r \approx 0.7$ (note that χ_ϕ cannot be determined in the region of $\nabla\omega_\phi \sim 0$).

Now, we have all the elements that we need in the model for calculating intrinsic rotation profiles. The results for the two ECH discharges of 1.0 MW and 1.7 MW heating power are presented in Fig. 10, which show quantitatively good agreement between the predicted intrinsic rotation profile and experimentally measured main ion toroidal rotation. It is worth noticing that the fluctuation level and turbulence driven transport, including residual stress at the saturated steady state, display some variations (see, for instance, the middle of Fig. 4). The Prandtl number may also vary within a certain range under different plasma conditions. As shown in Fig. 9, the time averaged Prandtl number exhibits some radial variation around its average value. How do all these impact the rotation prediction? To address this issue, we have carried out uncertainty quantification analysis, and the results are presented in the left panel of Fig. 10. First, different time windows are used for calculating the time-averaged steady state residual stress profile $\Pi^{\rm rs}_{r,\phi}(r)$ and thermal diffusivity profile $\chi_i(\rho)$ that are needed in Eq. (3) for calculating the rotation profile. As indicated by the solid magenta curve and solid black curve in the plot, corresponding to using a time window starting from $t = 400$ and $t = 500$, respectively, the result of predicted rotation is not sensitive to the time window used for time average. Moreover, the impact of uncertainty in the value of the Prandtl number on intrinsic rotation prediction is also assessed. Also plotted on the left of Fig. 10 are intrinsic rotation profiles reconstructed with variations of the Prandtl number $P_r = 0.7\pm0.1$ incorporating reasonable ranges around the averaged value observed in the gyrokinetic simulations. It is shown that quantitative agreement between the prediction and the measurement is insensitive to the Prandtl number variation over a reasonable range that is physically expected.

These DIII-D ECH discharges are formed with an upper-single-null shape. The up-down asymmetry in the magnetic geometry may cause a shift in turbulence maximum away from the low field side mid-plane, which breaks the odd symmetry in the momentum flux between the upper and lower parts of the plasma in the local limit, leading to a non-vanishing, net momentum flux.[18] In the right panel of Fig. 10, predictions are made for both up-down symmetry and up-down asymmetry magnetohydrodynamical (MHD) equilibria in order to examine the effect of up-down asymmetry associated with the upper-single-null geometry. The up-down symmetric MHD equilibrium is generated using the same experimental profiles of pressure and current as that of the up-down asymmetric equilibrium but with the up-down asymmetry on the last magnetic surface boundary (from experimental data of the magnetic measurement) removed. The minor difference observed in the predicted intrinsic rotation profile suggests that the effect of up-down asymmetry in the equilibrium on turbulence driven residual stress is insignificant in those DIII-D plasmas. It is possible that stronger up-down asymmetry may enhance its effect and, in particular, in the edge region.

The intrinsic rotation developed in the low power phase of ECH heated plasmas is significantly different than that in the higher power phase, as shown in the left panel of Fig. 11. More specifically, the core intrinsic rotation in the 0.5 MW phase is low and with a flat profile. Our gyrokinetic simulation and analysis have been extended to the low power phase, attempting to understand the underlying causes for the difference. The right panel of Fig. 11 presents the result of total low-k mode intensity in the linear phase (after modes grow for many e-foldings in amplitude) from a global GTS simulation that includes all low-k modes in the ITG-TEM range. It is found that the low-k modes are mostly stable over a wide range of plasma minor radii except in a narrow, deep-core region around $\rho = 0.25$. The consistent result is also shown in the TGLF analysis of this plasma.[6] The low-k linear stability is due to the flatter ion temperature profile at 0.5 MW (see Fig. 1), and this observation is well outside of experimental error bars. In fact, the ion thermal transport inferred from the experiment for this plasma is near the

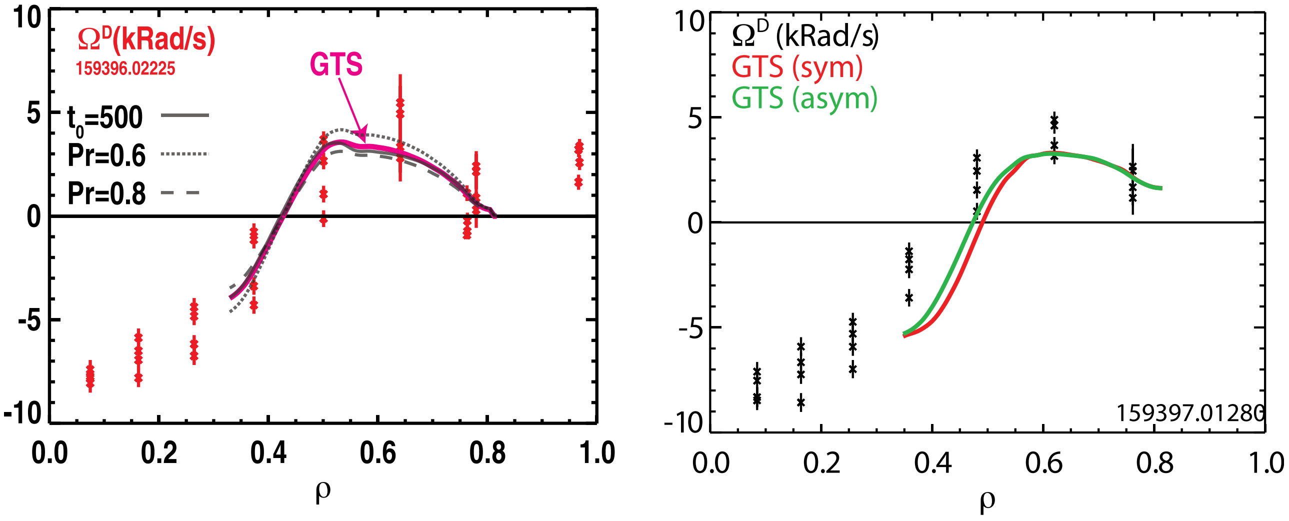

FIG. 10. Radial profile of predicted intrinsic rotation compared with experimentally measured main ion toroidal rotation for two DIII-D ECH plasmas at input powers of 1.0 MW (left) and 1.7 MW (right). In the left panel, also plotted are predictions using a different time window for obtaining steady state residual stress and thermal diffusivity and using Prandtl numbers $P_r = 0.7\pm0.1$ (within a variation of GTS simulation). In the right panel, red and green lines are predicted intrinsic rotations based on GTS simulations using up-down symmetry and asymmetry equilibrium, respectively.

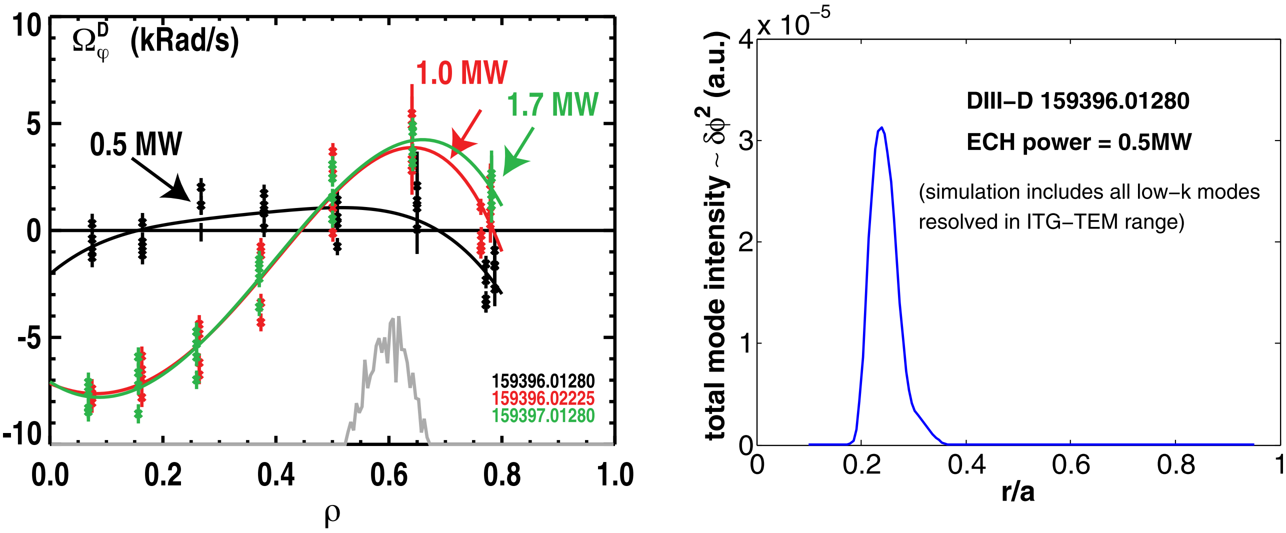

FIG. 11. Radial profiles of measured main ion toroidal rotation at different ECH input powers (left) and the radial profile of total low-k mode intensity in the linear phase (after modes grow for many e-foldings in amplitude) from a global GTS simulation of the low ECH power phase (0.5 MW) (left).

neoclassical level within experimental error bars, which is consistent with the lack of low-k instability observed in both GTS and TGLF simulations. Given that the momentum transport (both diffusive and non-diffusive) produced by low-k turbulence is needed to bring momentum from the edge to the core and to redistribute it, and thus to form a global rotation profile, it seems quite reasonable that the lack of specific low-k turbulence, which is presented in the higher power phase, would result in a weak core intrinsic rotation generation during the low power phase. When turbulence is negligible, neoclassical physics can play a role. While it is well known that the neoclassical toroidal momentum flux is very small compared to the neoclassical heat flux,[17,36] the neoclassical toroidal viscosity, however, may come into play when the toroidal symmetry is broken by magnetic perturbations (driven either internally or externally). This should be further investigated in the future.

Finally, we point out that the quantitative agreement obtained between the first-principles-based predictions and experimental measurements for a set of discharges with varying ECH power is non-trivial and meaningful. To a certain extent, it provides a test and verification for the physics mechanism of turbulence-driven intrinsic rotation, key mechanisms for $k_\parallel$-symmetry breaking for turbulence to generate residual stress, and global gyrokinetic simulation model for calculating momentum transport.

IV. CHARACTERISTIC DEPENDENCE OF INTRINSIC THE ROTATION PROFILE STRUCTURE

The rotation amplitude and profile structure (e.g., rotation gradient) have different effects on MHD stability and microturbulence. One important question to ask is what determines the radial structure of the residual stress and associated intrinsic rotation profile. Through the well-known radial force balance relation, $E_r = \frac{1}{ne}\frac{\partial p}{\partial r} + \frac{1}{c}\left(B_\theta V_\phi - B_\phi V_\theta\right)$, both the pressure gradient and toroidal rotation contribute to the equilibrium radial electric field E_r. In terms of $\mathbf{E} \times \mathbf{B}$ flow generation, it is then highly interesting to know whether intrinsic rotation works against or in concert with the pressure gradient and/or externally driven rotation, in contributing to the mean $\mathbf{E} \times \mathbf{B}$ shearing rate. As a typical example, it has been long observed in experiments that the addition of ECH to co-injection NBI-driven plasmas results in an apparently ECH-induced "counter-torque."[37] The experimental observations which are considered to be associated with the effects of ECH-induced turbulence-driven intrinsic torque include a reduction in toroidal rotation velocity and flattening of the rotation profile[38,39] relative to that of purely NBI-driven plasmas. Therefore, understanding the characteristic dependence of the residual stress profile structure will help us develop a possible approach for flow control and optimization. In particular, understanding the intrinsic rotation reversal phenomenon, which has been widely observed in various experiments,[40–42] is of great interest.[39] Given that there are multiple physics mechanisms for $k_\parallel$-symmetry breaking, which may coexist and compete with each other in different parametric regimes, one general remark is that the radial structure of residual stress and intrinsic rotation seem to show a complicated dependence on multiple physics parameters, such as the turbulence type (for example, ITG vs TEM), q-profile structure (magnetic shear, q-value), and collisionality.

Here, we first use the predictive model described above to examine the magnetic shear effect on intrinsic rotation reversal. Experimental observations in lower hybrid current drive (LHCD) plasmas on Alcator C-MOD suggest that an intrinsic rotation reversal can be linked to the change in the q-profile.[42] The underlying mechanism may be linked to the effect of magnetic shear on the turbulence spectrum.[22,43] Figure 12 presents the results of two simulations of collisionless TEM (CTEM) turbulence using the same density and temperature profiles for electrons (ions) but different equilibria with key differences in the q-profile. More specifically, one equilibrium has normal shear, while the other has a weak, close to zero, shear in the inner core region (see the right panel of Fig. 12). The pressure profile and boundary surface used for generating the two equilibria are the same.

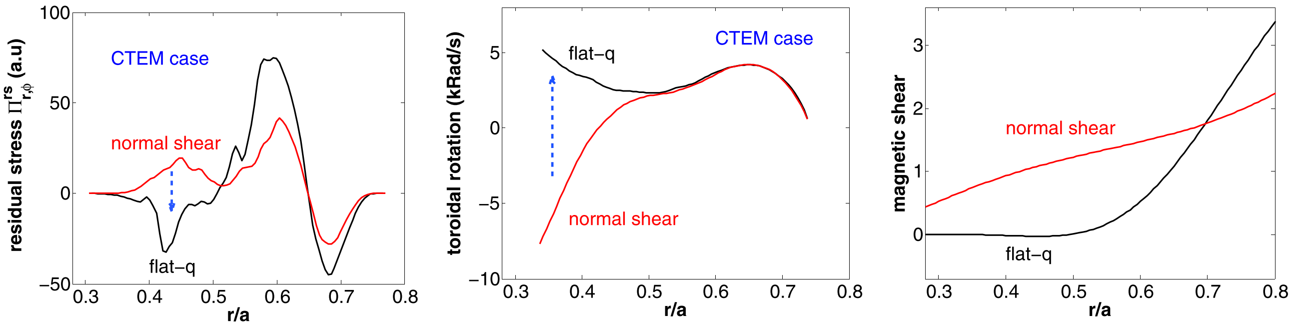

FIG. 12. Radial profiles of CTEM turbulence driven residual stress (left), intrinsic rotation (middle) from two simulations using different q-profiles in equilibria, and magnetic shear of the two equilibria (right).

As shown in the left panel of Fig. 12, the CTEM-driven residual stress is found to bifurcate in the inner core region as the q-profile changes from normal to weak (or zero) shear. Correspondingly, the CTEM-driven intrinsic rotation reverses in that region (see the middle panel of Fig. 12). The underlying physics is linked to magnetic shear effects on the turbulence spectrum. It is found that the global eigenmodes of ITG and TEM show a radial shift in poloidal mode harmonics due to the synergic effect of toroidal coupling and intensity gradient.[22,43] This results in $k_\parallel$-symmetry breaking and is a distinct mechanism from that of the $\mathbf{E}\times\mathbf{B}$-shear induced radial shift.[16] Because weaker magnetic shear makes the radial shift more significant, this new mechanism becomes important in the low magnetic shear regime and may lead to intrinsic rotation reversal as magnetic shear changes. As a result, it introduces a critical value of magnetic shear for the reversal of the residual stress orientation and consequently the reversal of intrinsic rotation. The critical magnetic shear for intrinsic rotation reversal is found to be $\sim$0.3 in the CTEM regime.[43] Furthermore, Fig. 12 shows that the intrinsic rotations generated in the two cases are almost the same in the outer core region, while the amplitude of CTEM-driven residual stress is significantly lower in the normal shear case. This result highlights the fact that it is the ratio of $\Pi^{\rm rs}_{r,\phi}/\chi_\phi$ (or $\Pi^{\rm rs}_{r,\phi}/\chi_i$) rather than the magnitude of the residual stress itself, which is critical for determining the intrinsic rotation. Based on this, one may anticipate that any effects of fluctuations that influence turbulence-driven ion thermal flux and residual stress in a different way can strongly impact intrinsic rotation profile formation. Finally, another interesting observation is that intrinsic rotation developed in the core region with weak magnetic shear tends to have a flatter profile (smaller gradient) relative to the normal shear case. This can be seen in the middle panel of Fig. 12 for CTEM-driven rotation. This seems to be the case for ITG-driven intrinsic rotation as well, as indicated in Fig. 13, which plots the radial profiles of $\Pi^{\rm rs}_{r,\phi}/\chi_i$ obtained for ITG turbulence from two simulations. The two ITG simulations are carried out using the same two equilibria as for the CTEM simulations presented in Fig. 12. Since the rotation gradient is proportional to $\Pi^{\rm rs}_{r,\phi}/\chi_i$, the significantly smaller amplitude of $\Pi^{\rm rs}_{r,\phi}/\chi_i$ observed for the flat q-profile relative to the normal shear q-profile indicates that the ITG-driven rotation shear is significantly smaller for the flat q-profile.

The change in underlying turbulence, e.g., from ITG to TEM, is also considered as a possible mechanism responsible for the intrinsic rotation reversal observed in experiments. This is mostly based on quasilinear arguments and the properties of linear modes. More specifically, the intrinsic rotation reversal is linked to the properties that i) the poloidal tilt of global mode structure switches orientation and ii) the mode propagation changes from the ion to electron diamagnetic direction as turbulence changes from ITG and TEM. Figure 14 shows the radial profiles of residual stress produced by the ITG and CTEM modes in the linear phase of two GTS simulations with the same MHD equilibrium. Indeed, the residual stress profiles of ITG and CTEM modes show the opposite orientation. However, nonlinear physics may significantly change the properties of turbulent fluctuations, and it is not clear whether such quasilinear properties of residual stress are still applicable in the nonlinear turbulence state. Our nonlinear, global simulations show that the switch of underlying turbulence from ITG to TEM does not generally induce an intrinsic rotation reversal. A rotation reversal during an ITG → TEM transition also depends on other plasma conditions. Figure 15 shows an ITG → TEM induced intrinsic rotation reversal which is observed in weak magnetic shear regime (not generally observed). The underlying dynamics is again associated with the sign change of finite $k_\parallel$ (the right panel of Fig. 15) and the fluctuation-generated stress (middle panel) during ITG → TEM transition in weak magnetic shear.

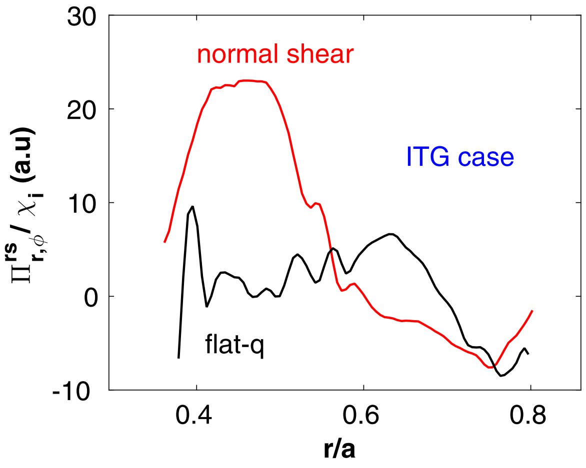

FIG. 13. Radial profiles of $\Pi^{\rm rs}_{r,\phi}/\chi_i$ obtained for ITG turbulence from two simulations using the same two equilibria with different q-profiles as that of Fig. 12.

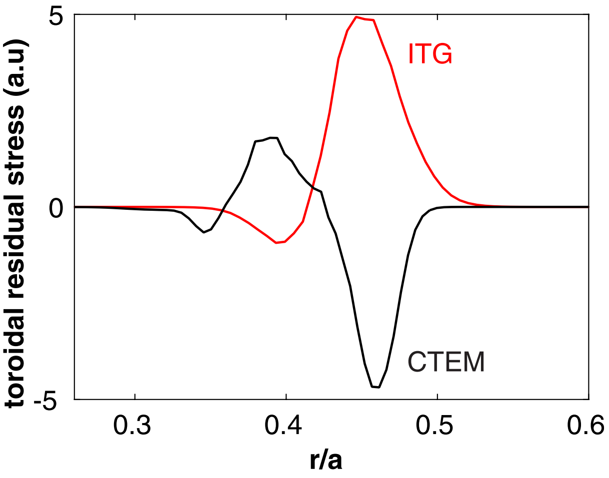

FIG. 14. Radial profile of residual stress produced by ITG and CTEM modes in the linear phase from two simulations with the same equilibrium.

V. SUMMARY

This paper reports on progress in studying intrinsic rotation physics in magnetic fusion through global nonlinear gyrokinetic simulations and the development of a first-principles-based model for predicting the intrinsic rotation profile in experiments. The validation study carried out here focuses on understanding the profile structure of intrinsic rotation in electron heated DIII-D experiments through ECH. A non-monotonic intrinsic rotation profile with an off-axis peak is typically observed to form in the core region of those ECH plasmas. It is shown for the first time that turbulent fluctuation-driven momentum transport can account for both the shape and magnitude of the observed intrinsic toroidal rotation profile. Specifically, nonlinear, global gyrokinetic simulations show that significant ITG turbulence is driven in those ECH plasmas as ECH input power increases. Although ECH directly heats electrons, strong collisional coupling in low temperature situations can effectively transfer core-injected ECH power to ions and build up sufficient free energy in the ion temperature profile to excite ion turbulence in the core region. The ITG turbulence, while producing anomalous thermal transport of the experimental level in those ECH discharges, is also found to drive a substantial non-diffusive momentum flux along with the diffusive momentum flux around a mid-radius-peaked intrinsic toroidal rotation profile. The non-diffusive momentum flux is comparable to the momentum diffusion in amplitude and dominated by the residual stress with a negligible contribution from the momentum pinch. Importantly, the residual stress profile shows a robust anti-gradient, dipole structure in a set of ECH discharges with varying ECH power, which is essentially a mirror image of the simulated diffusive momentum flux profile. Such interesting features of non-diffusive momentum fluxes, in connection with edge momentum sources and sinks, are found to be critical to drive the non-monotonic core rotation profiles observed in the experiments. Simulation results indicate that the major contribution to the toroidal residual stress is from the parallel Reynolds stress, through which various physics effects play a role in producing $k_\parallel$-asymmetry in the fluctuation spectrum. It appears that the residual stress profile structure formed in those ECH plasmas is largely determined by the dipole structure presented in the spectral-averaged $k_\parallel$ of fluctuations. Both the turbulence intensity gradient and zonal flow $\mathbf{E} \times \mathbf{B}$ shear are identified as major contributors to the generation of the $k_\parallel$-asymmetry needed for the residual stress generation. By balancing the residual stress and the momentum diffusion, a self-organized, steady-state rotation profile is calculated. The predicted core rotation profiles agree well with the experimental measurements for a set of ECH discharges with varying input power. Quantitative analysis has been carried out to assess the impact of errors in the Prandtl number and the simulated, time-averaged steady-state transport fluxes on the rotation prediction. It is shown that the agreement between the simulation predictions and the experiments is not sensitive to the errors in those parameters over the range observed in simulations.

The structure of the residual stress profile depends on the details of the fluctuation spectrum, which can reverse, depending on, e.g., the type of turbulence and q-profile structure and thus can naturally lead to intrinsic rotation reversals as observed in many experiments with different plasma conditions. The characteristic dependence of the residual stress structure on the multi-dimensional parametric space covering the turbulence type, q-profile structure, and up-down asymmetry in magnetic geometry has been studied using our first-principles-based predictive model with the goal of developing the physics understanding needed for rotation profile control and optimization. It is shown that the up-down asymmetry in magnetic equilibrium associated with the up-single-null divertor geometry in the DIII-D ECH

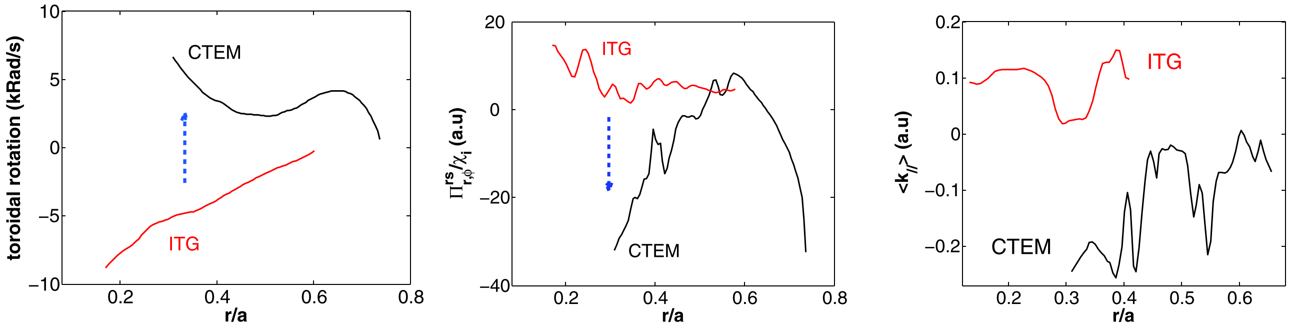

FIG. 15. Radial profile of fluctuation driven intrinsic rotations (left), the ratio of residual stress and thermal diffusivity (middle), and spectral averaged $\langle k_\parallel \rangle$ (right) due to ITG and CTEM turbulence with a flat-q profile in equilibrium.

experiments does not significantly affect the turbulence-driven residual stress in the core region and the associated core intrinsic rotation structure (given that the edge rotation velocity remains unchanged). It is found that CTEM-driven intrinsic rotation can bifurcate (namely, reverse) when the q-profile changes from weak to normal shear in the core region. Furthermore, the switch of the underlying turbulence from ITG to TEM does not necessarily result in an intrinsic rotation reversal as suggested by simple quasilinear argument. On the other hand, an intrinsic rotation reversal induced by ITG-TEM transition is observed in the flat-q profile regime.

ACKNOWLEDGMENTS

Various useful discussions with Dr. G. M. Staebler, Dr. D. J. Battaglia, Dr. J. A. Boedo, Dr. J. S. deGrassie, Dr. W. M. Solomon, Dr. Z. Lu, Dr. R. Hawryluk, Dr. R. Nazikian, and Dr. Y. Ren are acknowledged. The authors Wang and Grierson are grateful to Dr. R. Hawryluk and Dr. R. Nazikian for encouragement. This work was supported by U.S. DOE under Contract Nos. DE-AC02-09CH11466 and DE-FC02-04ER54698. Simulations were performed on Edison at the National Energy Research Scientific Computing Center (NERSC). DIII-D data shown in this paper can be obtained in digital format by following the links at https://fusion.gat.com/global/D3D_DMP.

[1] J. A. Boedo, J. S. deGrassie, B. Grierson, T. Stoltzfus-Dueck, D. J. Battaglia, D. L. Rudakov, E. A. Belli, R. J. Groebner, E. Hollmann, C. Lasnier, W. M. Solomon, E. A. Unterberg, J. Watkins, and D.-D. Team, Phys. Plasmas **23**, 092506 (2016).

[2] T. Stoltzfus-Dueck, Phys. Rev. Lett. **108**, 065002 (2012).

[3] N. Fedorzak, P. H. Diamond, G. Tynan, and P. Manz, Nucl. Fusion **52**, 103013 (2012).

[4] B. LaBombard, J. E. Rice, A. E. Hubbard, J. W. Hughes, M. Greenwald, J. Irby, Y. Lin, B. Lipschultz, E. Marmar, C. Pitcher, N. Smick, S. Wolfe, S. Wukitch, and the Alcator Group, Nucl. Fusion **44**, 1047 (2004).

[5] E. J. Doyle, W. A. Houlberg, Y. Kamada, V. Mukhovatov, T. H. Osborne, A. Polevoi, G. Bateman, J. W. Connor, J. G. Cordey, T. Fujita *et al.*, Nucl. Fusion **47**, S18 (2007).

[6] B. A. Grierson, W. X. Wang, S. Ethier, G. M. Staebler, D. J. Battaglia, J. A. Boedo, J. S. deGrassie, and W. M. Solomon, Phys. Rev. Lett. **118**, 015002 (2017).

[7] J. S. deGrassie, K. H. Burrell, L. R. Baylor, W. Houlberg, and J. Lohr, Phys. Plasmas **11**, 4323 (2004).

[8] J. S. deGrassie, J. E. Rice, K. H. Burrell, R. J. Groebner, and W. M. Solomon, Phys. Plasmas **14**, 056115 (2007).

[9] B. A. Grierson, K. H. Burrell, C. Chrystal, R. J. Groebner, D. H. Kaplan, W. Heidbrink, J. M. M. Burgos, N. A. Pablant, W. M. Solomon, and M. A. V. Zeeland, Rev. Sci. Instrum. **83**, 10D529 (2012).

[10] B. A. Grierson, K. H. Burrell, W. Heidbrink, M. J. Lanctot, N. A. Pablant, and W. M. Solomon, Phys. Plasmas **19**, 056107 (2012).

[11] W. X. Wang, Z. Lin, W. M. Tang, W. W. Lee, S. Ethier, J. L. V. Lewandowski, G. Rewoldt, T. S. Hahm, and J. Manickam, Phys. Plasmas **13**, 092505 (2006).

[12] W. X. Wang, P. H. Diamond, T. S. Hahm, S. Ethier, G. Rewoldt, and W. M. Tang, Phys. Plasmas **17**, 072511 (2010).

[13] W. X. Wang, S. Ethier, Y. Ren, S. Kaye, J. Chen, E. Startsev, Z. Lu, and Z. Q. Li, Phys. Plasmas **22**, 102509 (2015).

[14] P. H. Diamond, C. J. McDevitt, O. D. Gurcan, T. S. Hahm, and V. Naulin, Phys. Plasmas **15**, 012303 (2008).

[15] R. Dominguez and G. M. Staebler, Phys. Fluids B **5**, 3876 (1993).

[16] O. D. Gurcan, P. H. Diamond, T. S. Hahm, and R. Singh, Phys. Plasmas **14**, 042306 (2007).

[17] W. X. Wang, T. S. Hahm, S. Ethier, G. Rewoldt, W. Lee, W. M. Tang, S. M. Kaye, and P. H. Diamond, Phys. Rev. Lett. **102**, 035005 (2009).

[18] Y. Camenen, A. G. Peeters, C. Angioni, F. J. Casson, W. A. Hornsby, A. P. Snodin, and D. Strintzi, Phys. Plasmas **16**, 062501 (2009).

[19] O. D. Gurcan, P. H. Diamond, P. Hennequin, C. J. McDevitt, X. Garbet, and C. Bourdelle, Phys. Plasmas **17**, 112309 (2010).

[20] Y. Camenen, Y. Idomura, S. Jolliet, and A. G. Peeters, Nucl. Fusion **51**, 073039 (2011).

[21] R. E. Waltz, G. M. Staebler, and W. M. Solomon, Phys. Plasmas **18**, 042504 (2011).

[22] Z. X. Lu, W. X. Wang, P. Diamond, G. Tynan, S. Ethier, C. Gao, and J. Rice, Phys. Plasmas **22**, 055705 (2015).

[23] F. I. Parra, M. Barnes, and A. G. Peeters, Phys. Plasmas **18**, 062501 (2011).

[24] T. S. Hahm and K. H. Burrell, Phys. Plasmas **2**, 1648 (1995).

[25] J. Candy and R. E. Waltz, Phys. Rev. Lett. **91**, 045001 (2003).

[26] W. X. Wang, T. S. Hahm, S. Ethier, G. Rewoldt, W. W. Lee, W. M. Tang, S. M. Kaye, and P. H. Diamond, in *Proceedings of the 22nd IAEA Fusion Energy Conference*, Geneva, Switzerland (IAEA Vienna, 2008), Paper No. IAEA-CN-165/TH-P8-44.

[27] B. F. McMillan, S. Jolliet, T. M. Tran, L. Villard, A. Bottino, and P. Angelino, Phys. Plasmas **16**, 022310 (2009).

[28] Y. Idomura, H. Urano, N. Aiba, and S. Tokuda, Nucl. Fusion **49**, 065029 (2009).

[29] Y. H. Xu, S. Jachmich, R. R. Weynants, A. Huber, B. Unterberg, and U. Samm, Phys. Plasmas **11**, 5413 (2004).

[30] A. Politzer, Phys. Rev. Lett. **84**, 1192 (2000).

[31] P. Bak, C. Tang, and K. Wiesenfeld, Phys. Rev. Lett **59**, 381 (1987).

[32] N. Mattor and P. H. Diamond, Phys. Fluids **31**, 1180 (1988).

[33] A. G. Peeters, C. Angioni, and the ASDEX Upgrade Team, Phys. Plasmas **12**, 072515 (2005).

[34] F. J. Casson, A. G. Peeters, Y. Camenen, W. A. Hornsby, A. P. Snodin, D. Strintzi, and G. Szepesi, Phys. Plasmas **16**, 092303 (2009).

[35] J. C. Hillesheim, F. I. Parra, M. Barnes, N. A. Crocker, H. Meyer, W. A. Peebles, R. Scannell, and A. Thornton, and the MAST Team. Nucl. Fusion **55**, 032003 (2015).

[36] S. M. Kaye, W. Solomon, R. E. Bell, B. P. LeBlanc, F. Levinton, J. Menard, G. Rewoldt, S. Sabbagh, W. Wang, and H. Yuh, Nucl. Fusion **49**, 045010 (2009).

[37] W. M. Solomon, K. H. Burrell, J. S. deGrassie, J. A. Boedo, A. M. Garofalo, R. A. Moyer, S. H. Muller, C. C. Petty, and H. Reimerdes, Nucl. Fusion **51**, 073010 (2011).

[38] K. Ida, T. Minami, Y. Yoshimura, A. Fujisawa, C. Suzuki, S. Okamura, S. Nishimura, M. Isobe, H. Iguchi, K. Itoh, S. Kado, Y. Liang, I. Nomura, M. Osakabe, C. Takahashi, K. Tanaka, and K. Matsuoka, Phys. Rev. Lett. **86**, 3040 (2001).

[39] P. Diamond, Y. Kosuga, O. Gurcan, C. McDevitt, T. Hahm, N. Fedorczak, J. Rice, W. Wang, S. Ku, J. Kwon, G. Dif-Pradalier, J. Abiteboul, L. Wang, W. Ko, Y. Shi, K. Ida, W. Solomon, H. Jhang, S. Kim, S. Yi, S. Ko, Y. Sarazin, R. Singh, and C. Chang, Nucl. Fusion **53**, 104019 (2013).

[40] A. Bortolon, B. Duval, A. Pochelon, and A. Scarabosio, Phys. Rev. Lett. **97**, 235003 (2006).

[41] J. E. Rice, I. Cziegler, P. H. Diamond, B. P. Duval, Y. A. Podpaly, M. L. Reinke, P. C. Ennever, M. J. Greenwald, J. W. Hughes, Y. Ma, E. S. Marmar, M. Porkolab, N. Tsujii, and S. M. Wolfe, Phys. Rev. Lett. **107**, 265001 (2011).

[42] J. E. Rice, Y. A. Podpaly, M. L. Reinke, R. Mumgaard, S. D. Scott, S. Shiraiwa, G. M. Wallace, B. Chouli, C. Fenzi-Bonizec, M. F. F. Nave *et al.*, Phys. Rev. Lett. **111**, 125003 (2013).

[43] Z. X. Lu, W. X. Wang, P. Diamond, G. Tynan, S. Ethier, J. Chen, C. Gao, and J. Rice, Nucl. Fusion **55**, 093012 (2015).